Journal of Materials Chemistry A

ARTICLE

Hole Transporting Materials Based on Benzodithiophene and Dithienopyrrole Cores for Efficient Perovskite Solar Cells

Received 00th January 20xx,
Accepted 00th January 20xx

DOI: 10.1039/x0xx00000x

www.rsc.org/

R. Sandoval-Torrientes,[a] I. Zimmermann,[b] J. Calbo,[c] J. Aragó,[c] J. Santos,[a] E. Ortí,*[c] N. Martín*[a,d] and M. K. Nazeeruddin*[b]

The development of highly efficient hole transporting materials (HTMs) for perovskite solar cells (PSCs) is still one of the most thrilling research subjects in the development of this emerging photovoltaic technology. Inner ring engineering of the aromatic core of new HTMs –consisting in three fused rings endowed with four triarylamine units– reveals major performance effects over the fabricated devices. In particular, substitution of the central pyrrole ring in dithienopyrrole (DTP) by a benzene ring –benzodithiophene (BDT)– allows enhancing the power conversion efficiency from 15.6% to 18.1%, in devices employing mixed-perovskite $(FAPbI_3)_{0.85}(MAPbBr_3)_{0.15}$ (MA: $CH_3NH_3^+$, FA: $NH{=}CHNH_3^+$) under 1 sun illumination. In comparison, 2,2′,7,7′-tetrakis(*N*,*N*-di-*p*-methoxyphenylamine)-9,9′-spirobifluorene (spiro-OMeTAD) yielded 17.7%. The novel HTM molecules show an efficient quenching of the perovskite photoluminescence, indicating an efficient charge transfer from the active layer to the HTM, along with a good conductivity (comparable to that of spiro-OMeTAD reference). Density functional theory (DFT) calculations allowed rationalizing the electrochemical and optical properties, and predict a reorganization energy (λ) for the best performing BDT-based HTM (0.101 eV) significantly lower than that computed for the benchmark spiro-OMeTAD (0.139 eV).

1. Introduction

Among the different strategies utilized to harness solar energy, the photovoltaic (PV) approach is the only one able to directly convert Sun's light into electrical energy. The over-all PV capacity installed in 2015 was calculated to be 227.1 GW, which represents 0.6% of the global power generation.[1] Virtually, all the installed PV capacity relies on silicon-based solar cells (SCs). Despite the dramatic reduction of the production costs, quality PV silicon production still represents an enormous energetic burden. The so-called emerging PV technologies (organic cells, quantum dot cells, perovskite cells, etc.) are promising future alternatives that aim to fulfill niche markets where silicon cells cannot compete, when not directly competing with conventional silicon based SCs. Among these emerging technologies, perovskite solar cells are seriously positioning themselves as competitor candidates to silicon solar cells. No more than seven years after they were first reported by Kojima *et al.*,[2] perovskite solar cells (PSCs) already reach efficiencies exceeding 22%,[3] competitive with the well-established silicon SCs, which is an unprecedented development in the field of photovoltaics.

Current research on PSCs focuses on two well-differentiated approaches, the first one searching the modification of the photo-active perovskite layer. Manipulation of perovskite's ABX_3 structure by anionic and cationic substitution allows controlling its absorption properties. Modifying the size of the organic A cation has been observed to have a measurable effect on the band gap. Substitution of methylammonium (MA) by formamidinium (FA) leads to a nearly 0.1 eV gap narrowing.[4] Replacement of Pb^{2+} by Sn^{2+} (cation B) has also demonstrated to substantially affect the light absorption capabilities, allowing band gaps as narrow as 1.20 eV for $MASnI_3$.[5] However, the most significant band gap manipulations have been achieved by substitution of the halide anion X. The lattice changes induced by increasing size of the halide anion (Cl < Br < I) reduce the band gap and result in a spectral shift towards longer wavelengths.[2,6] The combination of the aforementioned structural and electronic modifications in mixed compositional perovskites such as $MAPb(I_{1-x}Br_x)_3$, $Cs_x(MA_{0.17}FA_{0.83})_{(100-x)}Pb(I_{0.83}Br_{0.17})_3$ or $[FAPbI_3]_{0.85}[MAPbBr_3]_{0.15}$ has redounded in perovskites with enhanced stability rendering efficiencies up to 22%.[3,7,8,9]

The second major approach in PSCs concerns the synthesis and development of new and more efficient, both in terms of cost and performance, charge transporting materials. Examples of electron transporting materials (ETMs) employing azaacenes[10,11] or fullerene derivatives[12–14] have been reported in order to replace the TiO_2 as the archetype ETM. More importantly, hole transporting materials (HTMs) research may be considered as one of the main topics in PSCs as the field is still dominated by the expensive compound 2,2′,7,7′-

[a] IMDEA-Nanociencia, Ciudad Universitaria de Cantoblanco, Madrid, 28049, Spain.
[b] EPFL VALAIS, Sion, 1951, Switzerland.
[c] Instituto de Ciencia Molecular, Universidad de Valencia, Paterna, 46980, Spain.
[d] Facultad de Ciencias Químicas, Universidad Complutense de Madrid, Madrid, 28040, Spain.

Electronic Supplementary Information (ESI) available: Synthetic and computational details, device fabrication and characterisation, and supplementary figures. See DOI: 10.1039/x0xx00000x

tetrakis(*N*,*N*-di-*p*-methoxyphenylamine)-9,9′-spirobifluorene (spiro-OMeTAD).[15,16] So far, a high number of new HTMs has been tested making use of many types of chemical structures and constituents. Nevertheless, it may be unquestionably asserted that structures exhibiting triarylamine functionalities are the most successful and repeated ones. The reason for this success lies in the highest-occupied molecular orbital (HOMO) energy levels this functionality provides, that allows efficient overlapping with the perovskite's valence band. Triarylamines have been conjugated to spiranic central cores resembling that of spiro-OMeTAD, delivering efficiencies comparable to spiro-OMeTAD or even superior.[17–20] Being aware that energy matching is not the only concurring criteria, much attention has been devoted to developing novel central cores able to promote efficient crystalline ordering. Well-ordered hole transporting layers (HTLs) allow efficient charge transport and extraction to the electrodes, and motifs that promote aggregation (aromatic surfaces for π–π stacking, sulphur heteroatoms for S···S interactions, etc.) have been demonstrated to be very effective.[21–25]

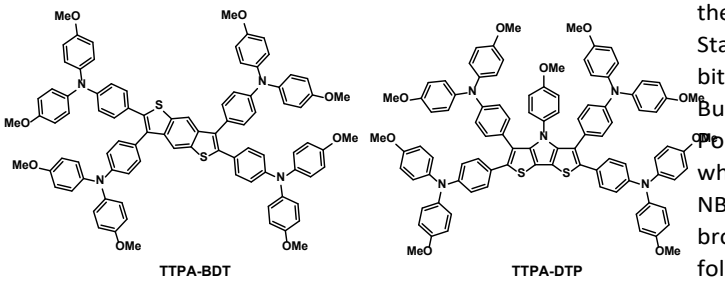

Fig. 1 Molecular structures of the HTMs based on the use of benzodithiophene (BDT) and dithienopyrrole (DTP) as cores bearing four triphenylamine (TPA) moieties.

Electron rich molecules like benzodithiophene (BDT) and dithienopyrrole (DTP) have been widely employed in organic photovoltaics with varying degree of success.[26–28] These two building-blocks offer structural elements, like having large π-conjugated surfaces and the presence of heteroatoms, that help promoting intermolecular interactions. Furthermore, the two thiophene rings that both molecules possess bear the potential of being substituted with up to four triarylamine moieties. Combined all together, these characteristics prompted us with the idea of designing two new molecules for their use as HTMs in PSCs, where BDT and DTP central cores are substituted with four *N*,*N*-bis(4-methoxyphenyl)aniline units through the 2- and 3-positions of the thiophene rings giving rise to the tetrakistriphenylamine (TTPA) derivatives sketched in **Fig. 1**. The substitution of the inner core benzene ring of BDT by a pyrrole ring in DTP allows adding an extra heteroatom to the system, along with providing a stronger electron donating character. The PSCs fabricated making use of these two materials as HTLs show efficient charge transport to the electrodes that allows obtaining photocurrent conversion efficiencies (PCEs) over 18%.

In order to gain a better understanding of the structural and electronic properties of the new BDT and DPT derivatives, density functional theory (DFT) calculations were performed at the B3LYP/6-31G** level. Interestingly, the predicted reorganization energy for the best performing BDT-based HTM (0.101 eV) resulted to be significantly lower than that computed for the benchmark spiro-OMeTAD (0.139 eV).

2. Results and Discussion

2.1. Materials Synthesis and Properties

The synthesis of the new HTMs was carried out as shown in **Scheme 1** with good yields. Molecule **TTPA-DTP** was obtained in a straightforward manner comprising four synthetic steps; the DTP central core was attained following a modification of the procedure reported by Wong and collaborators.[29] Starting from commercially available 3,3′-dibromo-2,2′-bithiophene, the DTP core is obtained in moderate yield by a Buchwald-Hartwig cross-coupling reaction with *p*-anisidine. Polybromination of the DTP core is achieved in the form of a white insoluble solid after one-pot sequential treatment with NBS at room temperature, followed by reflux after addition of bromine. The final product **TTPA-DTP** is accomplished by a four-fold Suzuki-Miyaura reaction with four equivalents of *p*-methoxytriphenylaminepinacol boronate (**4**). On the other hand, **TTPA-BDT** was prepared in two steps from commercially available dibenzothiophene, consisting in tetrabromination by treatment with excess of bromine, followed by a four-fold Suzuki-Miyaura reaction with boron pinacolate **4**. The structural characterization of the synthesized products was consistent with the molecular formulae of **TTPA-DTP** and **TTPA-BDT**. Full characterization and synthetic details of the products is provided in the Electronic Supplementary Information (ESI).

To gain more insight into the structural and electronic properties of the BDT and DPT derivatives, density functional theory (DFT) calculations were performed at the B3LYP/6-31G** level for the **TTPA-BDT** and **TTPA-DTP** compounds in the presence of the solvent (CH_2Cl_2). Their respective cores (BDT and DTP), the pendant triarylamine (TPA) moiety, and the reference spiro-OMeTAD compound were also computed for comparison purposes (see the Supporting Information for full computational details).

Journal of Materials Chemistry A

ARTICLE

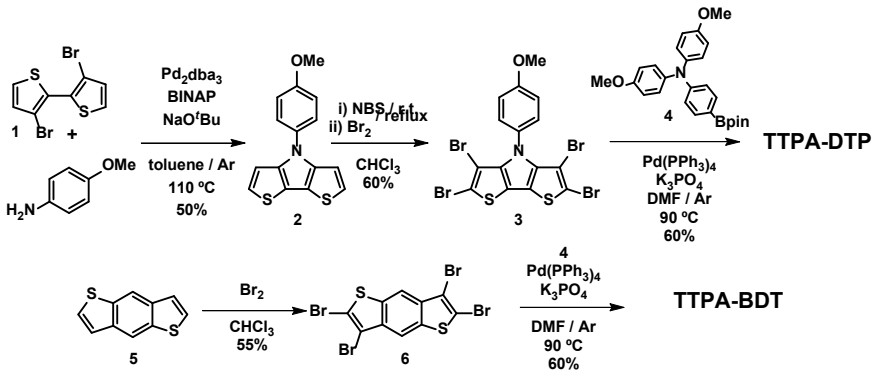

Scheme 1. Synthetic route for the preparation of the heterocyclic **TTPA-BDT** and **TTPA-DTP** HTMs.

Fig. S1 collects the most representative bond length values calculated at the B3LYP/6-31G** level for the BDT and DPT cores and the **TTPA-BDT** and **TTPA-DTP** HTMs. The central benzene ring of the C_{2h}-symmetry BDT core mostly preserves its delocalized structure with carbon–carbon (CC) bond distances between 1.390 and 1.427 Å. The terminal thiophene rings lose part of their typical structural pattern with alternating single and double CC bonds showing a significant difference between the terminal CC double bond (1.356 Å) and the bond fused to the benzene ring (1.427 Å). In contrast, the DTP core exhibits a clear single–double CC alternating backbone similar to that found for other related thiophene oligomers.[30,31] The insertion of the TPA units to obtain **TTPA-BDT** and **TTPA-DTP** hardly causes any substantial change in the bond distances of the cores, with the exception of the terminal CC and carbon–sulfur bonds (Fig. S1).

Fig. 2 shows the frontier molecular orbitals computed for the TPA unit, the BDT and DPT cores, the **TTPA-BDT** and **TTPA-DTP** HTMs and the spiro-OMeTAD reference compound. The topology of the HOMO of **TTPA-BDT** and **TTPA-DTP** clearly resembles that obtained for the corresponding cores with important contributions from the TPA moieties attached to the 2-position of the thiophene rings, especially in the case of **TTPA-DTP**. The HOMOs of the pristine BDT and DTP cores, calculated at −5.55 and −5.30 eV, respectively, undergo a noticeable destabilization in passing to **TTPA-BDT** (−4.62 eV) and **TTPA-DTP** (−4.51 eV) upon the insertion of the strong electron-donating TPA moieties. This enhancement of the electron-donor character brings the HOMOs of the **TTPA-BDT** and **TTPA-DTP** HTMs close to that calculated for the reference spiro-OMeTAD (−4.44 eV). It is important to notice that a significant charge transfer occurs from the peripheral TPA groups to the central cores, which hold a total net charge of −0.30e and −0.22e for **TTPA-BDT** and **TTPA-DTP**, respectively. The electronic structure of the **TTPA-BDT** and **TTPA-DTP** HTMs is therefore found to be remarkably polarized.

Journal of Materials Chemistry A

ARTICLE

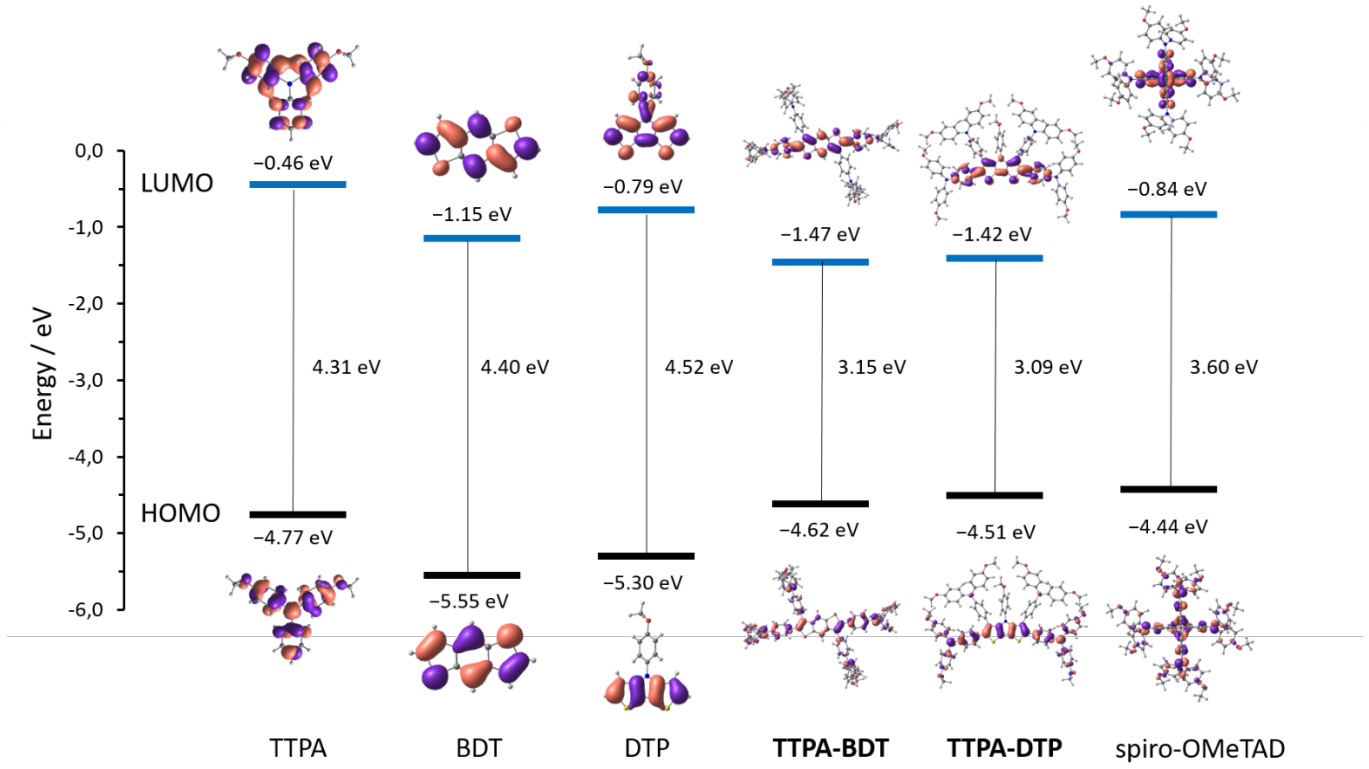

Fig. 2 Energy diagram displaying the frontier molecular orbitals computed at the B3LYP/6-31G** level for the TPA unit, the BDT and DTP cores, the **TTPA-BDT** and **TTPA-DTP** HTMs, and the reference spiro-OMeTAD.

The electrochemical properties of the sulfur-rich **TTPA-BDT** and **TTPA-DTP** HTMs were studied by cyclic voltammetry (CV) in CH_2Cl_2 solution (**Fig. 3a**). CV experiments evidence the reductive character expected from these electron-rich materials. Compound **TTPA-BDT** presents a quasireversible oxidation process ($E_{1/2}^{ox}$ = 0.92 V *vs.* NHE), that shows a subtle shoulder which is rationalized as the sequential oxidation of the two TPA moieties fully conjugated with the core (linked to the BDT through the thiophene 2- and 2'-positions), followed by the oxidation of the TPAs attached to the thiophene 3- and 3'-positions. This apparent subtlety makes the 2,2' TPAs being stronger donors due to their effective conjugation with the BDT core, in line with the HOMO computed for **TTPA-BDT** localized at the core and the 2,2' TPAs. In contrast, derivative **TTPA-DTP** has a much richer redox activity, showing up to four quasireversible oxidation waves ($E_{1/2}^{ox}$ = 0.54, 0.71, 0.91, and 1.20 V *vs.* NHE). In this case, the lower oxidation potentials are ascribed to the better electron-donor properties of the DTP core, which is expected to participate in the oxidation process. The third oxidation wave (0.95 V) seems to be more intense and probably arises from the TPA moieties attached to the DTP through thiophene 3,3'-positions, which, as for **TTPA-BDT**, cannot experience an effective conjugation with the core. This difference in donating strengths is reflected in the HOMO energies estimated from the oxidation potentials, obtaining –5.36 eV for **TTPA-BDT** and –4.98 eV for **TTPA-DTP**. In comparison, spiro-OMeTAD presents a HOMO level of –5.16 eV.[32] The HOMO level observed for **TTPA-BDT** is closer in energy to the valence band of the perovskite (*ca.* –5.65 eV), which enables a more efficient hole extraction, with consequences over the overall performance of the PSC devices built.

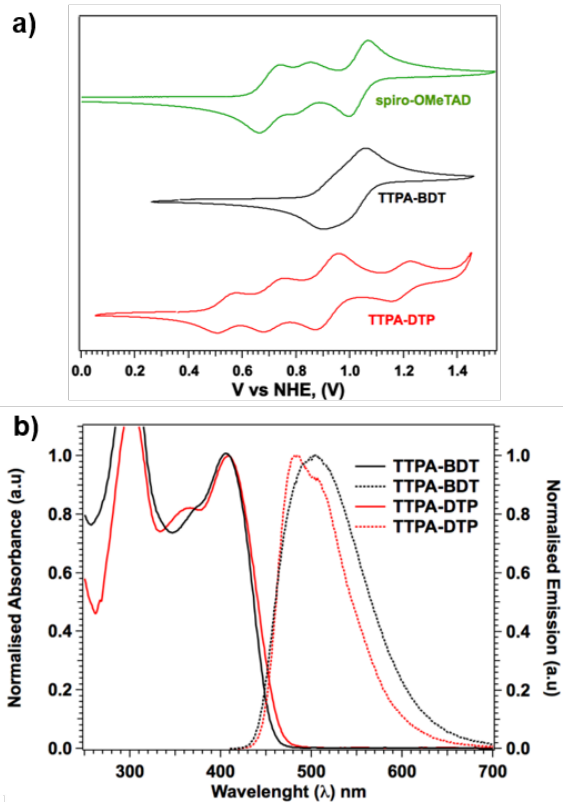

Fig. 3 a) Cyclic voltammograms of **TTPA-BDT** and **TTPA-DTP** recorded in CH_2Cl_2 solution at a scan rate of 100 mV s^{-1}. b) Normalized absorption and emission spectra of **TTPA-BDT** and **TTPA-DTP** recorded in CH_2Cl_2 solution.

Table 1 Electrochemical and optical properties of **TTPA-BDT** and **TTPA-DTP**.

HTM	$E_{1/2}^{ox}$ [V][a]	E_{HOMO} [eV][b]	λ_{max}^{abs} [nm]	λ_{max}^{ems} [nm]	$E_{0\text{-}0}$ [eV][c]	E_{LUMO} [eV][d]
TTPA-BDT	0.92	–5.36	408	505	2.73	–2.63
TTPA-DTP	0.54	–4.98	407	485	2.76	–2.22

[a] Measured *vs.* normal hydrogen electrode (NHE). [b] E_{HOMO} estimated as E_{HOMO} = –4.44 eV – $E_{1/2}^{ox}$. [c] Optical band gap estimated from the intersection of the absorption and emission spectra. [d] E_{LUMO} estimated as $E_{LUMO} = E_{HOMO} + E_{0\text{-}0}$.

To gain a better understanding of the electrochemical properties of the HTMs studied, the oxidized species (up to the tetracation) of **TTPA-BDT** and **TTPA-DTP** were also calculated at the B3LYP/6-31G** level in CH_2Cl_2. **Table S1** collects the charges accumulated by the constituting fragments (central cores and TPA units) as oxidation occurs. The evolution of the charges upon oxidation indicates that for the cation species the charge is initially extracted from the TPA units (especially from those linked to the 2.2'-positions of the thiophene rings) with significant contributions from the central BDT and DTP cores. This effect is more pronounced for **TTPA-DTP**, for which the conjugation through the central core is more effective. Upon further oxidation (dication, trication and tetracations), the charge is gradually extracted from all the TPA units. The evolution of the charges extracted (Table S1) evidences the most favorable electronic communication between the TPA moieties introduced in 2,2'-positions and the conjugated BDT and DTP cores. It should be noted that, for **TTPA-BDT**, the ionization energies (IEs) required for passing from the neutral molecule to the cation (IE1), from the cation to the dication (IE2), from the dication to the trication (IE3) and from the trication to the tetracation (IE4) are predicted to have relatively close values (4.56, 4.79, 5.09 and 5.17 eV, respectively). The difference in IE values is smaller between IE1 and IE2 (0.22 eV) and especially between IE3 and IE4 (0.08 eV). These differences explain the electrochemical behavior found for **TTPA-BDT** showing a unique four-electron oxidation wave with a shoulder at low potentials corresponding to the first two oxidation processes (Fig. 3a). In contrast, **TTPA-DTP**, which presents a stronger donor character with a smaller IE1 value (4.37 eV) in line with the electronic properties discussed above, exhibits a larger separation of 0.46 eV between the IE1 and IE2 (4.83 eV) energies, whereas IE3 (5.10 eV) and IE4 (5.21 eV) remain quite close at 0.11 eV. These ionization energies justify the well-separated oxidation waves, the third one implying a two-electron process, registered for **TTPA-BDT** (Fig. 3a). The fourth oxidation wave of **TTPA-DTP** recorded at 1.22 V should mainly correspond to the oxidation of the DTP core. Theoretical calculations therefore clarify the different electrochemical behavior found for **TTPA-BDT** and **TTPA-DTP**.

Hole reorganization energies (λ) were calculated at the B3LYP/6-31G** level in gas phase to evaluate the capability of the **TTPA-BDT** and **TTPA-DTP** compounds as HTMs (see the Supporting Information for full computational details). The λ values estimated for **TTPA-BDT** and **TTPA-DTP** are 0.101 and 0.285 eV, respectively. Note that these λ values are significantly smaller than those obtained for their corresponding fragments (0.166, 0.467 and 0.274 eV for BDT, DTP and TPA, respectively) due to the fact that charge extraction involves both the core and the peripheral TPA moieties (especially those linked through the 2,2'-positions of the thiophene rings). **TTPA-BDT** exhibits a low reorganization energy similar to those found for other excellent *p*-type semiconducting organic materials[33,34] and smaller than that obtained for the reference spiro-OMeTAD (0.139 eV) at the B3LYP/6-31G** level of theory.[24] **TTPA-DTP** shows a higher reorganization energy because the formation of the cation implies important changes in the single-double CC bond-length alternation pattern of the DTP core. Therefore, **TTPA-BDT** presents a great potential as hole transporting material for PSC devices owing to its small λ value and the appropriate energy level alignment with the valence band edge of the perovskite.

Despite the electrochemical differences found between **TTPA-BDT** and **TTPA-DTP**, both HTMs show very similar absorption profiles with strong absorption features below 470 nm (**Fig. 3b**). Both systems exhibit a broad band covering the 250–470 nm range with two well-resolved peaks. The first peak is registered at *ca.* 407 nm (6.5 and 8.9 × 10^4 $M^{-1}cm^{-1}$ for **TTPA-BDT** and **TTPA-DTP**, respectively) along with a shoulder in the 360–370 nm range. The second intense absorption peak is observed at around 310 nm. Theoretical simulations of the absorption spectra for **TTPA-BDT** and **TTPA-DTP** (**Fig. S5**) were performed from B3LYP/6-31G** time-dependent DFT (TDDFT) calculations of the lowest-energy singlet excited electronic states (S_n) in the presence of CH_2Cl_2 (**Table S2**). The theoretical spectra correctly

reproduce the experimental absorption spectra with two intense bands calculated at 448 and 305 nm (**TTPA-BDT**) and 463 and 307 nm (**TTPA-DTP**). For **TTPA-BDT**, the band at 448 nm results from the $S_0 \rightarrow S_1$ and $S_0 \rightarrow S_3$ electronic transitions calculated at 450 and 414 nm, respectively, and gives rise to the experimental peak registered at 407 nm. These $S_0 \rightarrow S_1$ and $S_0 \rightarrow S_3$ transitions involve one-electron promotions from the HOMO−2 and HOMO to the LUMO, and imply some charge transfer from the peripheral TPA units to the central BDT moiety (**Fig. S3**). The band predicted at 305 nm, which is related to the experimental band peaking at 310 nm, shows a complex nature with significant participation of many electronic transitions. For **TTPA-DTP**, a similar absorption spectrum is predicted with slight bathochromic shifts of the absorption bands.

The emission spectra show broad bands centered at 505 and 485 nm for **TTPA-BDT** and **TTPA-DTP**, respectively. Optical band gaps of 2.73 and 2.76 eV (for **TTPA-BDT** and **TTPA-DTP**, respectively) are estimated from the intersection of the absorption and emission spectra.

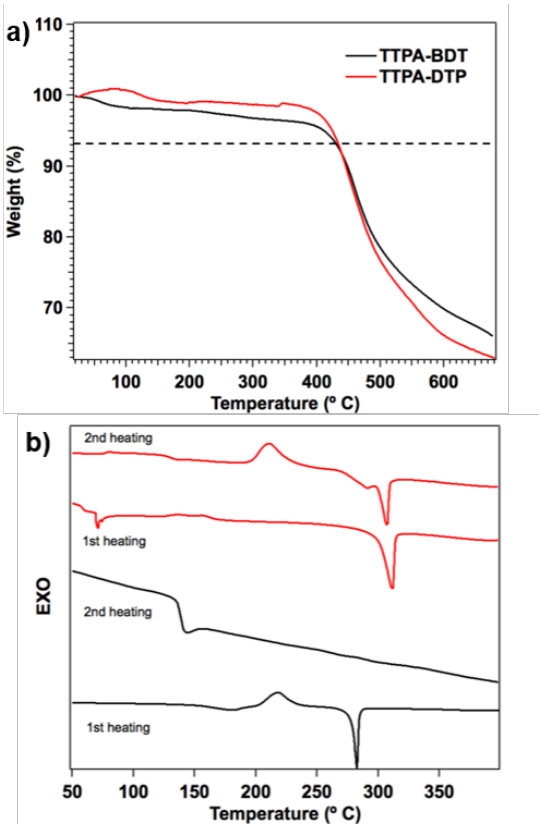

Fig. 4 a) Thermogravimetric analysis of the HTMs under nitrogen at a heating rate of 10 °C min^{-1}. b) Differential scanning calorimetry of **TTPA-DTP** (red) and **TTPA-BDT** (black) under nitrogen at a heating rate of 20 °C min^{-1} (1^{st} and 2^{nd} cycle).

The thermal properties of the HTMs were determined by thermogravimetric analysis (TGA) and differential scanning calorimetry (DSC) (**Fig. 4**). Both **TTPA-BDT** and **TTPA-DTP** show good thermal stability displaying a plateau until 411.7 and 424.7 °C, respectively, when they start decomposing. Upon heating, the BDT-based compound shows a glass transition at 164.3 °C prior to experiencing a crystallization process at 218.3 °C, eventually melting at 282.5 °C during the first heating cycle. The second heating cycle just shows a lower temperature glass transition at around 138.5 °C. Similarly, the DTP-based material experiences a glass transition at 71.1 °C, followed by two crystallization processes at 105.3 and 156.1 °C, to finally melt at 311.5 °C, during the first heating cycle. In the second cycle, the material undergoes a glass transition at 112.8 °C, to further crystallize at 211.1 °C and melt at 306.9 °C.

2.2. Photovoltaic Characterization

The new hole transporting materials **TTPA-BDT** and **TTPA-DTP** were employed in perovskite-based solar cells to compare their performance with the most commonly used compound spiro-OMeTAD as a reference. PSCs were prepared following the standard n-i-p configuration having a stack of fluorine-doped tin oxide (FTO) conductive glass|compact titania (30 nm)|mesoporous titania (200 nm)|perovskite (600 nm)|HTM (50–300 nm|gold electrode (70 nm). Owing to the exceptional advantages it presents, the compositional modification $(MAPbBr_3)_{0.15}(FAPbI_3)_{0.85}$ previously introduced by Seok *et al.* was used for the photoactive perovskite layer.[9] The perovskite layer was fabricated following a one-step spin-coating procedure involving anti-solvent treatment. The HTMs were applied by spin-coating their corresponding solutions in chlorobenzene onto the annealed perovskite film. Tert-butylpyrydine, lithium tris[bis(trifluoromethylsulfonyl)imide] (Li-TFSI) and tris[2-(1H-pyrazol-1-yl)-4-tert-butylpyridine]cobalt(III) (FK209) were added in equimolar amounts as additives to all HTMs solutions. Detailed description of the solar cell fabrication process can be found in the Supporting Information. **Fig. 5a** shows a cross-section scanning electron microscopy (SEM) image of a typical solar cell prepared using the aforementioned solar cell configuration. For both molecules, **TTPA-BDT** and **TTPA-DTP**, the thickness of the HTM layer for the best performing devices was shown to be between 50 and 100 nm, which is slightly thinner than the 300 nm that is usually observed in devices with spiro-OMeTAD, but consistent with other reports on alternative small molecule HTMs.[24] **Fig. 5b** shows the energy level diagram of the different solar cell components. Both HTMs, **TTPA-BDT** and **TTPA-DTP**, have their HOMO levels close to the valence band of the perovskite and should therefore be able to extract holes from the perovskite absorber.

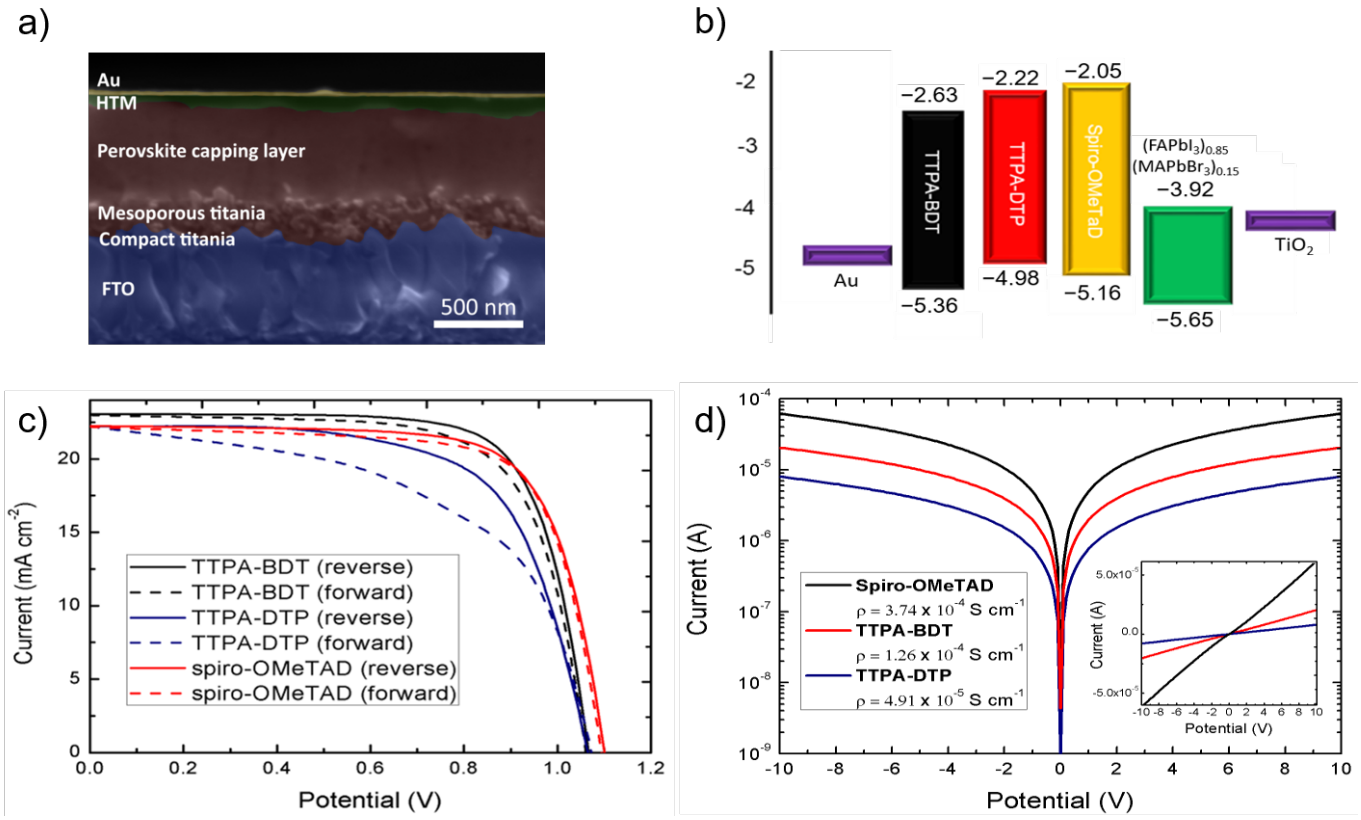

Fig. 5 a) Cross-sectional SEM image of a PSC fabricated with **TTPA-DTP** as HTM layer. b) Energy level diagram of the different solar cell components. c) Forward and reverse current density-voltage (*J*–*V*) plots of PSC devices measured under reverse bias employing different HTMs, *i.e.* **TTPA-BDT**, **TTPA-DTP** and spiro-OMeTAD as a reference. d) Current-voltage curves of **TTPA-BDT**, **TTPA-DTP** and spiro-OMeTAD as a reference measured on substrates having interdigitating gold electrodes with a channel length of 2.5 µm. Conductivity values were calculated using Ohms law.

Reverse and Forward current density-voltage (*J*–*V*) plots of the devices employing the different HTMs, along with the corresponding photovoltaic parameters of the champion cells, are respectively displayed in **Fig. 5c** and **Table 2**. The reference spiro-OMeTAD cells did not show any significant hysteresis, in contrast with the new HTMs; therefore, it may be concluded that the hysteresis observed for the cells employing **TTPA-BDT** and **TTPA-DTP** originates from the HTM layer. This behaviour may arise from an unbalanced charge extraction at the perovskite/HTM interface, as well as small pinholes that are present due to the non-uniform film.[35] With a power conversion efficiency (PCE) of 18.1%, measured under simulated sunlight (AM 1.5 G; 100 mW cm^{-1}), **TTPA-BDT** shows an excellent performance, similar to the reference compound spiro-OMeTAD (17.7%) (PCE values of the 15 devices fabricated per HTM are shown in **Fig. S9**). A high short circuit current of 23.0 mA cm^{-2} could be observed for **TTPA-BDT** compared to 22.3 mA cm^{-2} for spiro-OMeTAD. On the other hand, the open circuit voltage is 30 mV lower than the reference cell. **TTPA-DTP** with a PCE of 15.6% due to the relatively low fill factor caused by low conductivity. Although the HOMO level of the two molecules differs by around 400 meV, no significant difference in the V_{oc} of the devices could be observed. This can be related to the different electrochemical behavior observed for both HTMs: a unique four-electron oxidation wave for **TTPA-BDT** and a well-separated one-electron first oxidation wave for **TTPA-DTP**. In fact, the HOMO energies calculated theoretically for **TTPA-BDT** and **TTPA-DTP** differ in only 107 meV. One reason for the underperformance of the device using **TTPA-DTP** could be the poor solubility of this HTM in chlorobenzene, which leads to a less uniform film formation (see **Fig. S7**).

Table 2 Photovoltaic parameters of the champion PSCs.

HTM	V_{OC} [V]	J_{SC} [mA cm^{-2}]	*FF* [%]	*PCE* [%]
TTPA-BDT (reverse)	1.07	23.0	73.6	18.1
TTPA-BDT (forward)	1.06	23.0	70.0	17.2
TTPA-DTP (reverse)	1.07	22.2	65.8	15.6
TTPA-DTP (forward)	1.07	22.2	53.7	12.8
spiro-OMeTAD (reverse)	1.10	22.3	72.5	17.7
spiro-OMeTAD (forward)	1.10	22.2	72.4	17.6

To get further insight into the charge transport properties of the new HTMs, conductivity measurements were carried out. Spiro-OMeTAD, **TTPA-BDT** and **TTPA-DTP** were applied on interdigitated gold substrates by spin-coating their corresponding solutions in chlorobenzene. The molecules were doped using 6 mol% FK209, representing the same amount used in the devices. The results are shown in semi logarithmic *I*–*V* plots in **Fig. 5d** and the corresponding conductivity values were calculated using Ohms law. The highest conductivity value was

found for spiro-OMeTAD (3.74×10^{-4} S cm^{-1}) followed by **TTPA-BDT** (1.26×10^{-4} S cm^{-1}) and **TTPA-DTP** (4.91×10^{-5} S cm^{-1}). Compared to spiro-OMeTAD, the lower conductivity showed by **TTPA-BDT** is likely compensated by a thinner HTM layer, that in term yields a higher short circuit current (23.0 *vs.* 22.2 mA cm^{-2}). In contrast, in the case of **TTPA-DTP** the conductivity might be too low for an efficient charge extraction, thus adding further explanation for the lower device efficiency observed for this molecule. The smaller conductivity might be due to the higher reorganization energy calculated for **TTPA-DTP** (see above). From steady-state photoluminescence (PL) as well as transient PL we found that the new molecules behave in fact very similar. For both **TTPA-BDT** and **TTPA-DTP**, the steady state PL show an efficient quenching of the perovskite emission, evinced by a sharp decline of the curves within the 5–10 ns timescale (see **Figure S8**). Altogether, the PL behavior of the HTMs/perovskite blends is indicative of an efficient charge transfer from the active layer to the hole transporting layer which, in turn, is coherent with the good photovoltaic response of the devices built making use of **TTPA-BDT** and **TTPA-DTP**.

Conclusions

In summary, two novel electron-rich small molecules consisting in BDT and DTP aromatic cores, decorated each with four triarylamine moieties, have successfully demonstrated their functionality as efficient HTMs in perovskite-based photovoltaic devices. PL experiments evinced the ability of **TTPA-BDT** and **TTPA-DTP** to efficiently collect the holes generated within the perovskite active layer, rapidly quenching its fluorescence emission. From the photovoltaic performance of the devices built, it is concluded that the HTM featuring the BDT core (PCE = 18.1%) clearly not only outperformed the one bearing the DTP core (15.6%), but also bested the benchmark spiro-OMeTAD (17.7%). Despite showing a conductivity slightly lower than spiro-OMeTAD (1.26 *vs.* 3.74×10^{-4} S cm^{-1}), this particular **TTPA-BDT** HTM surpassed the spiro-OMeTAD performance due to a series of factors that include a better alignment of its HOMO (–5.36 eV) with the perovskite's valence band (–5.65 eV), and a significantly lower reorganization energy (0.101 eV). Another factor contributing to the better performance of **TTPA-BDT** is that the formed films showed thicknesses between 50 and 100 nm, quite below the typically observed for spiro-OMeTAD, which in turn contributes to its higher fill factor. From DFT calculations, **TTPA-DTP** is shown to present better electron-donor properties but also a higher reorganization energy (0.285 eV) that leads to a lower conductivity. We can therefore assume that HTMs based on triarylamines benefit from being fixed over a BDT aromatic core.

Conflicts of interest

There are no conflicts to declare.

Acknowledgements

This work was supported by the H2020-ICT-2014-1, grant agreement n°643791. We also thank the European Research Council (ERC-320441-Chir*all*carbon), the CAM (FOTOCARBON project S2013/MIT-2841) and the Spanish Ministry of Economy and Competitiveness MINECO (projects CTQ2014-52045-R, CTQ2015-71154-P, CTQ2016-81911-REDT, and Unidad de Excelencia María de Maeztu MDM-2015-0538), the Generalitat Valenciana (PROMETEO/2016/135) and European Feder funds (CTQ2015-71154-P). J.A. is grateful to MINECO for a "JdC-incorporación" post-doctoral fellowship. J.C. acknowledges the Generalitat Valenciana for a Vali+d post-doctoral fellowship. IMDEA Nanociencia acknowledges support from the 'Severo Ochoa' Programme for Centres of Excellence in R&D (MINECO, Grant SEV-2016-0686).

Notes and references

1 Source: International Energy Agency–Photovoltaic Power Systems Programme: www.iea-pvps.org.
2 A. Kojima, K. Teshima, Y. Shirai and T. Miyasaka, *J. Am. Chem. Soc.*, 2009, **131**, 6050−6051.
3 W. S. Yang, B.-W. Park, E. H. Jung, N. J. Jeon, Y. C. Kim, D. U. Lee, S. S. Shin, J. Seo, E. K. Kim, J. H. Noh and S. I. Seok, *Science,* 2017, **356**, 1376–1379.
4 G. E. Eperon, S. D. Stranks, C. Menelaou, M. B. Johnston, L. M. Herz and H. J. Snaith, *Energy Environ. Sci*., 2014, **7**, 982−988.
5 C. C. Stoumpos, C. D. Malliakas and M. G. Kanatzidis, *Inorg. Chem*., 2013, **52**, 9019−9038.
6 J. Calabrese, N. L. Jones, R. L. Harlow, N. Herron, D. L. Thorn and Y. Wang, *J. Am.Chem. Soc.*, 1991, **113**, 2328−2330.
7 J. H. Noh, S. H. Im, J. H. Heo, T. N. Mandal and S. I. Seok, *Nano Lett*., 2013, **13**, 1764−1769.
8 M. Saliba, T. Matsui, J.-Y. Seo, K. Domanski, J.-P. Correa-Baena, M. K. Nazeeruddin, S. M. Zakeeruddin, W. Tress, A. Abate, A. Hagfeldt and M. Gratzel, *Energy Environ. Sci.*, 2016, **9**, 1989.
9 N. J. Jeon, J. H. Noh, W. S. Yang, Y. C. Kim, S. Ryu, J. Seo and S. I. Seok, *Nature*, 2015, **517**, 476.
10 P.-Y. Gu, N. Wang, A. Wu, Z. Wang, M. Tian, Z. Fu, X. W. Sun and Q. Zhang, *Chem. Asian J.*, 2016, **11**, 2135.
11 D. Zhao, Z. Zhu, M.-Y. Kuo, C.-C. Chueh and A. K.-Y. Jen, *Angew. Chem. Int. Ed.*, 2016, **55**, 8999–9003.
12 Y. Zhong, R. Munir, A. H. Balawi, A. D. Sheikh, L. Yu, M.-C. Tang, H. Hu, F. Laquai and A. Amassian, *ACS Energy Lett.*, 2016, **1**, 1049–1056.
13 B. L. Watson, N. Rolston, K. A. Bush, T. Leijtens, M. D. McGehee and R. H. Dauskardt, *ACS Appl. Mater. Interfaces*, 2016, **8**, 25896–25904.
14 R. Sandoval-Torrientes, J. Pascual, I. García-Benito, S. Collavini, I. Kosta, R. Tena-Zaera, N. Martín and J. L. Delgado, *ChemSusChem*, 2017, **10**, 2023 –2029.
15 H. S. Kim, C. R. Lee, J. H. Im, K. B. Lee, T. Moehl, A. Marchioro, S. J. Moon, R. Humphry-Baker, J. H. Yum, J. E. Moser, M. Grätzel and N. G. Park, *Sci. Rep*., 2012, **2**, 591.
16 M. M. Lee, J. Teuscher, T. Miyasaka, T. N. Murakami and H. J. Snaith, *Science*, 2012, **338**, 643−647.
17 P. Ganesan, K. Fu, P. Gao, I. Raabe, K. Schenk, R. Scopelliti, J. Luo, L. H. Wong, M. Grätzel and M. K. Nazeeruddin, *Energy Environ. Sci*., 2015, **8**, 1986−1991.
18 D. Bi, B. Xu, P. Gao, L. Sun, M. Grätzel and A. Hagfeldt, *Nano Energy*, 2016, **23**,138−144.

19 Y.-K. Wang, Z.-C. Yuan, G.-Z. Shi, Y.-X. Li, Q. Li, F. Hui, B.-Q. Sun, Z.-Q. Jiang and L.-S. Liao, *Adv. Funct. Mater*., 2016, **26**, 1375−1381.

20 M. Saliba, S. Orlandi, T. Matsui, S. Aghazada, M. Cavazzini, J.-P. Correa-Baena, P. Gao, R. Scopelliti, E. Mosconi, K. H. Dahmen, F. De Angelis, A. Abate, A. Hagfeldt, G. Pozzi, M. Grätzel and M. K. Nazeeruddin, *Nature Energy*, 2016, **1**, 15017.

21 S. Kazim, F. J. Ramos, P. Gao, M. K. Nazeeruddin, M. Grätzel and S. Ahmad, *Energy Environ. Sci.*, 2015, **8**, 1816.

22 J. Cao, Y. M. Liu, X. Jing, J. Yin, J. Li, B. Xu, Y. Z. Tan and N. Zheng, *J. Am. Chem. Soc.*, 2015, **137**, 10914–10917.

23 A. Molina-Ontoria, I. Zimmermann, I. Garcia-Benito, P. Gratia, C. Roldan-Carmona, S. Aghazada, M. Grätzel, M. K. Nazeeruddin and N. Martín*, Angew. Chem. Int. Ed*., 2016, **55**, 6270−6274.

24 I. Zimmermann, J. Urieta-Mora, P. Gratia, J. Aragó, G. Grancini, A. Molina-Ontoria, E. Ortí, N. Martín and M. K. Nazeeruddin, *Adv. Energy Mater*., 2017, **7**, 1601674.

25 I. García-Benito, I. Zimmermann, J. Urieta-Mora, J. Aragó, A. Molina-Ontoria, E. Ortí, N. Martín and M. K. Nazeeruddin, *J. Mater. Chem. A*, 2017, **5**, 8317–8324.

26 L. Yuan, Y. Zhao, J. Zhang, Y. Zhang, L. Zhu, K. Lu, W. Yan and Z. Wei, *Adv. Mater*., 2015, **27**, 4229–4233.

27 M. Zhang, X. Guo, W. Ma, H. Ade and J. Hou, *Adv. Mater.*, 2015, **27**, 4655–4660.

28 C. D. Wessendorf, G. L. Schulz, A. Mishra, P. Kar, I. Ata, M. Weidelener, M. Urdanpilleta, J. Hanisch, E. Mena-Osteritz, M. Lindén, E. Ahlswede and P. Bäuerle, *Adv. Energy Mater*., 2014, **4**, 1400266.

29 H.-L. Wong, C.-C. Ko, W. H. Lam, N. Zhu and V. W.-W. Yam, *Chem. Eur. J.*, 2009, **15**, 10005–10009.

30 J. Aragó, P. M. Viruela, J. Gierschner, E. Ortí and B. Milián-Medina, *Phys. Chem. Chem. Phys.*, 2011, **13**, 1457–65.

31 J. Aragó, R. Ponce Ortiz, B. Nieto-Ortega, V. Hernández, J. Casado, A. Facchetti, T. J. Marks, P. M. Viruela, E. Ortí and J. T. López Navarrete, *Chemphyschem*, 2012, **13**, 168–76.

32 K. Rakstys, M. Saliba, P. Gao, P. Gratia, E. Kamarauskas, S. Paek, V. Jankauskas and M. K. Nazeeruddin, *Angew. Chem. Int. Ed.*, 2016, **55**, 7464–7468.

33 A. N. Sokolov, S. Atahan-Evrenk, R. Mondal, H. B. Akkerman, R. S. Sánchez-Carrera, S. Granados-Focil, J. Schrier, S. C. B. Mannsfeld, A. P. Zoombelt, Z. Bao and A. Aspuru- Guzik, *Nat. Commun.*, 2011, **2**, 437.

34 Y. Yao, H. Dong and W. Hu, *Adv. Mater.*, 2016, **28**, 4513–4523.

35 V. W. Bergmann, S. A. L. Weber, F. J. Ramos, M. K. Nazeeruddin, M. Grätzel, D. Li, A. L. Domanski, I. Lieberwirth, S. Ahmad and R. Berger, *Nat. Commun.*, 2014, **5**, 5001.